Numerical Studies of Wave Propagation in Polycrystalline Shape Memory Alloy Rods

Dimitris C. Lagoudas and Peter Popov
Department of Aerospace Engineering, Texas A&M University, TX 77843-3141, USA

ABSTRACT

Shape Memory Alloys (SMAs) have recently been considered for various applications involving dynamic loading. An SMA body subjected to external dynamic loading will experience large inelastic deformations that will propagate as phase transformation and/or detwinning shock waves. The wave propagation problem in a cylindrical SMA is studied numerically. An adaptive Finite Element Method (FEM) is used to solve several model problems representing various boundary conditions and thermomechanical paths. The mesh adaptivity is based on the Zienkiewicz-Zhu (ZZ) error estimator. Convergence studies are performed demonstrating the ability of the adaptive FEM to accurately and efficiently capture solutions with moving shock discontinuities. The energy dissipation capabilities of SMA rods are evaluated based on the numerical simulations. Correlations with existing experimental data on impact loading of NiTi SMA bars are also performed.

Keywords: S hape Memory Alloy, Dynamic Analysis, Adaptive FEM

1. INTRODUCTION

There are many areas of applications which can successfully utilize the unique properties of SMAs. The hysteretic response of polycrystalline SMA materials gives rise to different types of nonlinear wave propagation phenomena which can be successfully utilized to attenuate large impact loads and dissipate their energy. The research presented in this paper relates directly to the design of SMA components capable of absorbing dynamic loads. Such components can be integrated into critical parts of structures that may need protection from impact loads. Examples include joints that connect the hull of an underwater vehicle with its internal structure, tank armor or blast resistant cargo containers.

The two main characteristics of SMAs that can be used to achieve these aims are the *pseudoelastic* effect and the *shape memory effect*. At high temperatures the crystal lattice of a Shape Memory Alloy is in a high symmetry austenite phase (A). At low temperatures the material exists in a low symmetry martensite phase (M). Under the application of external stresses or changes in temperature a diffusionless phase transformation between these two phases takes place and causes the effect of *pseudoelasticity* (see [1]). Upon mechanical loading the material, after an initially linear response, develops large transformation strains which, upon the reversal of the loading are completely recovered. Thus mechanical energy is dissipated while no permanent strains remain in the material. The *Shape memory effect* allows material which has been deformed while in the martensitic phase to recover its shape upon heating. The mechanism behind this behavior is the ability of SMAs to allow for *detwinning* of the self-accomodated martensitic variants under application of external loads. Utilizing the shape memory effect also leads to dissipation of mechanical energy but the SMA has to be heated after the loading is applied to recover its shape.

An initial step into the analysis of the dynamic response of such structures is the understanding of the wave propagation phenomena in SMA rods. The nonlinear stress-strain response of the material significantly complicates the analytical analysis of the problem. Typically analytical solutions can be obtained by considering simple boundary conditions such as constant step-loading. This is done in [2] where the wave propagation problem is solved by the method of characteristics under adiabatic conditions. The stress-strain response of the material is modelled by the constitutive theory [3] developed for polycrystalline SMAs. A similar study involving a constant impact load, but focussing on different constitutive models which has been carried out in [4]. Both analytical solutions are developed and numerical simulations utilizing Finite Difference (FD) schemes are performed.

Numerical techniques are the only way to solve more complicated boundary value problems. An extensive study using different FD schemes is performed in [5]. The Lax-Friedrichs scheme was found to produce accurate

results but with large amounts of numerical dissipation. An adaptive Finite Element approach is successfully employed in [6] to obtaining accurate results for various thermomechanical loading conditions and boundary conditions. The numerical dissipation is controlled effectively by using appropriate time integrations schemes. Experimental results are also presented and compared with numerical simulations. A different approach is taken in [7] where the coupled problem of wave propagation and heat transfer in an SMA rod is investigated numerically. The authors focus on stress pulses of low magnitude that cause only elastic deformations. The temperature at one end of the SMA rod is chosen as a function of time in such a way as to utilize the phase change due to the shape memory effect in order to maximize the damping characteristics of the rod.

The selection of a proper constitutive model is essential to the analysis of the dynamic response of SMAs. Most of the early rate independent SMA models can be presented in a unified thermodynamic framework developed in [3] and based on the selection of appropriate thermodynamic potentials. This unified constitutive model is extended in [8] to incorporate transformation induced plastic deformations and to account for the evolution of the material behavior during cyclic loading. In the models proposed in [9; 10] the martensitic volume fraction is subdivided in two parts to account for thermally induced self-accommodated martensite and stress induced detwinned martensite. A different approach is taken in [11] where a rate dependent constitutive model is considered that allows for softening during phase transformation. In other studies [12; 13] micromechanical techniques are used to average the response of the parent austenitic phase and the different martensitic variants in order to obtain a model for the macroscopic behavior of polycrystalline SMAs. For further details on SMA models the reader is referred to [14]. In the current work the unified approach [3] is chosen over the more complex micromechanical models, assuming rate independence in the constitutive thermomechanical response of SMAs.

The main focus of this paper is the numerical study of the one-dimensional dynamic problem of loading an SMA rod. Based on the experimental observations in [6] the rate independent constitutive model [3] is selected. An adaptive FEM method is used to obtain numerical solutions of a step and pulse loading problems. The step loading problem is used to verify the rate of convergence of the FEM method utilizing known analytical results. The mesh adaptivity is based on the error estimator [15] which uses the gradient of the computed displacements to estimate the error locally. The estimator is applied at every time step to refine the FEM mesh in areas of the rod where the nonlinear wave interactions take place and coarsen it in regions of little or no disturbances. The computational savings achieved by the adaptive version of the FEM are also discussed. The impact pulse problem is solved in order to get a physically realistic picture of the wave propagation in SMA rods and to evaluate their energy dissipation capabilities. Finally, FE analysis of existing experimental results is performed and simulations are compared with experiments.

The paper begins with a brief overview in Section 2 of the field equations, boundary conditions and constitutive model defining the problem. Section 3 starts with an outline of the adaptive FEM used to simulate wave propagation in polycrystalline SMA rods. A model problem with a step-function stress boundary condition is next solved in Section 3.2. The problem is used to verify the numerical solution methodology and conduct convergence studies. Then, a square pulse impact problem is solved for conditions of stress induced martensite (Section 3.3). Expected values for energy dissipation as the pulse propagates through the rod are presented. Finally, in Section 3.4 the numerical schemes developed in this paper are utilized to simulate actual experimental results from a impact test on a NiTi SMA rod. The results of this work are discussed in Section 4.

2. FIELD EQUATIONS AND CONSTITUTIVE MODEL FOR THE IMPACT PROBLEM OF SMA RODS

A cylindrical SMA rod of uniform cross-section and length L is considered. Initially the rod is stress free and at rest and then is subjected to an impact load at its left end ($x = 0$). The right end ($x = L$) is assumed to remain traction free (Figure 1). The rod is assumed to be long compared to its diameter so it is under uniaxial stress state and the stress $\sigma(x, t)$ depends only on the axial position and time. The axial component of the displacement is denoted by $u(x, t)$. The density of the material ρ is assumed constant. Finally, due to the timescale of impact problems, adiabatic conditions are assumed in the rod. The local form of the balance of linear momentum and energy then become [16; 17]:

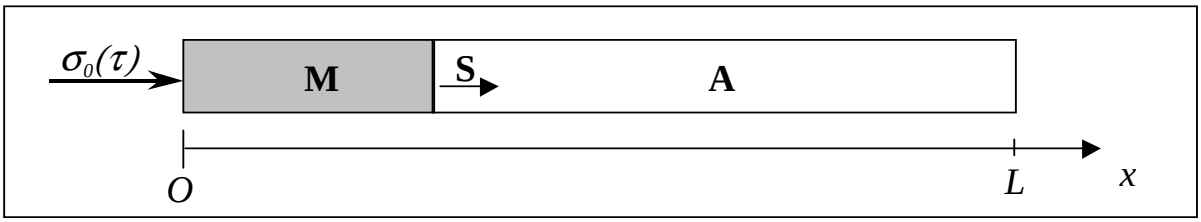

Figure 1. Schematic of the impact problem in an SMA rod.

$$\rho \frac{\partial^2 u}{\partial t^2} = \frac{\partial \sigma}{\partial x} \tag{1}$$

$$\rho \frac{\partial \mathcal{U}}{\partial t} = \sigma \frac{\partial^2 u}{\partial x \partial t} \tag{2}$$

where $\mathcal{U}$ is the internal energy per unit mass. The following initial and boundary conditions are further assumed:

$$u|_{t=0} = 0,\ \frac{\partial u}{\partial t}|_{t=0} = 0,\ T|_{t=0} = T_R \tag{3}$$

$$\sigma|_{x=0} = \sigma_0(t),\ \sigma|_{x=L} = 0 \tag{4}$$

The initial conditions indicate that the rod is at rest and its temperature $T(x,t)$ is equal to the ambient temperature T_R. The boundary conditions specify the traction $\sigma_0(t)$ applied to the left end of the rod. For a material initially in the austenitic phase **A**, the boundary traction typically causes the formation of a phase shock (denoted by S on Figure 1) that propagates along the length of the rod. The material located to the left of the shock has transformed and is in the martensitic phase **M**.

Equations (1)-(4) involve the field variables u, σ, $\mathcal{U}$ and T. Through the constitutive assumptions (see [6]) only $u(x,t)$ and the temperature $T(x,t)$ become the independent field variables. The constitutive model used to model the behavior of polycrystalline SMAs is formulated in terms of thermodynamic potentials and employs the volume fraction of detwinned martensite ξ formed from austenite as an internal variable [3]. The extension of this model which allows for the the modelling of the detwinning deformation is described in [6].

The adiabatic heat equation (2) can be simplified in order to facilitate the numerical treatment of the impact problem. Following the derivation in [6] it can be shown that under certain conditions the differential equation (2) can be solved explicitly to obtain

$$T = T_R e^{-\frac{1}{\rho c}(\alpha(\xi)\sigma + \rho \Delta s_0 \xi)} \tag{5}$$

where c is the specific heat, $\alpha(\xi)$ is the effective thermal expansion coefficient and $\Delta s_0 = s_0^M - s_0^A$, s_0^M and s_0^A being the specific entropies in the reference state for the martensitic and austenitic phase respectively. The impact problem then reduces to solving the balance of linear momentum (1) for the only field variable $u(x,t)$. The remaining field variables σ and T are coupled with the strain ε and the internal variable of the constitutive model ξ by the constitutive assumptions and equation (5).

3. ADAPTIVE FINITE ELEMENT ANALYSIS OF IMPACT LOADING OF AN SMA ROD

The numerical solution of wave propagation problems in nonlinear materials presents significant theoretical difficulties. A reliable FE analysis of such problems should be preceded by extensive numerical tests on boundary value problems with known analytical solutions. In this section the adaptive FEM procedure is briefly outlined followed by two numerical examples. The first example is the constant step loading problem which has been

Table 1. Material parameters used in the SMA model

Material constant	Description	Value
E^A	Young's modulus in austenite	70×10^9 Pa
E^M	Young's modulus in martensite	30×10^9 Pa
α^A	Thermal expansion coeff. in austenite	$22 \times 10^{-6}/K$
α^M	Thermal expansion coeff. in martensite	$10 \times 10^{-6}/K$
H	Maximal transformation strain	0.05
$\rho\Delta s_0$	Difference in the specific entropy of the two phases	$2 \times 10^5\ Pa/(m^3K)$
M^{of}	Martensitic start temperature	$275\ ^\circ K$
M^{os}	Martensitic finish temperature	$291\ ^\circ K$
A^{os}	Austenitic start temperature	$295\ ^\circ K$
A^{of}	Austenitic finish temperature	$315\ ^\circ K$

studied analytically (see [2; 4]). It is used to verify the convergence of the FEM and to demonstrate the capabilities of the adaptive mesh refinement strategy. Based on this results, a second problem with pulse boundary conditions is solved.

3.1. FEM procedure and mesh refinemnent

A standard semi-discrete Galerkin approximation with linear elements is used to generate the weak form of the boundary value problem. The boundary value problem is then reduced to a system of nonlinear ordinary differential equations. This system is in turn solved by the backward difference time integration scheme (see [18]). The overall structure of the numerical algorithm is comprised of an outer loop which performs the time marching of the ODEs, reducing them to a system of nonlinear algebraic equations at each step. Embedded in it is the Newton-Raphson iterative process which solves the system of nonlinear algebraic equations. At each step of the Newton algorithm the appropriate stiffness matrices and force vectors are assembled.

The computation of the stiffness matrices requires that the stress be evaluated at each integration point for given increments in strain and temperature. This is done with the help of the cutting plane return-mapping algorithm described in [19]. The coupling of the stress with the temperature in equation (5) results in the need of an additional iterative process described in [6] that finds a solution to both the heat equation and the dependence of the stress on strain and temperature that comes through the constitutive assumptions. This is a computationally very expensive operation which makes the assembly process the most time-consuming stage of the FEM procedure.

In order to reduce the computational time an adaptive meshing utilizing the Zienkiewicz-Zhu error estimator (see [15]) is used. The estimator evaluates the difference between the piecewise constant stresses of the FEM solution and their piecewise linear interpolation. This allows for local estimation of the error on the element level. The estimator is applied at the end of each Newton step. If the resulting mesh is fine enough and satisfies the target precision requirements the algorithm proceeds to the next time step. Otherwise the mesh is refined/coarsened and the time step is repeated.

3.2. Constant load impact problem

The first model problem to be considered is step loading under conditions of pseudoelasticity. The step loading problem is defined by the boundary condition

$$\sigma_0(t) = \begin{cases} 0 & \text{for } t \leq 0 \\ \sigma_0 & \text{for } t > 0 \end{cases} \tag{6}$$

This simple boundary condition makes the direct analytical solution to the problem possible (for a detailed discussion, see [2]) and is therefore a convenient starting point in analyzing the FEM method. The structure of the solution depends strongly on the impact stress σ_0. Let the pair $(\varepsilon_{el}, \sigma_{el})$ be the point on the hysteresis curve (Figure 2) that corresponds to the start of the phase transformation. In this example σ_0 it is taken to

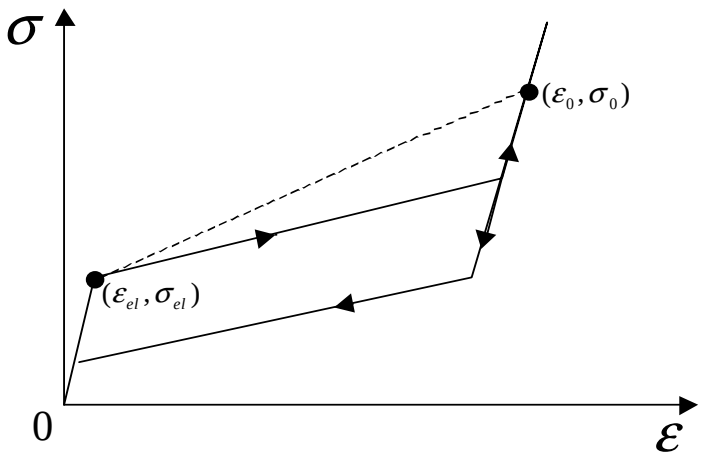

Figure 2. Schematic of a stress-strain hysteresis loop and the critical points defining the solution to constant step loading problem.

be sufficiently high so that full phase transformation transformation has occurred. It is also required that the value of σ_0 be high enough, so that the graph of of the stress strain relationship of the SMA is below the line connecting the points $(\varepsilon_{el}, \sigma_{el})$ and $(\varepsilon_0, \sigma_0)$. Following the analysis in [2; 4] the exact solution for the stresses has a two-shock structure:

$$\sigma(x,t) = \begin{cases} \sigma_0 & \text{for} \quad 0 \leq x/t \leq V_{ph} \\ \sigma_{el} & \text{for} \quad V_{ph} < x/t \leq V_{el} \\ 0 & \text{for} \quad V_{el} < x/t \end{cases} \tag{7}$$

The faster shock is a linear thermoelastic elastic shock and has velocity:

$$V_{el} = \sqrt{\frac{\sigma_{el}}{\rho \varepsilon_{el}}} \tag{8}$$

This shock is due to the shock type of the boundary condition and the initial linear stress-strain response. The second, slower shock, is a transformation shock which travels with velocity

$$V_{ph} = \sqrt{\frac{\sigma_0 - \sigma_{el}}{\rho(\varepsilon_0 - \varepsilon_{el})}} \tag{9}$$

This shock occurs not only because of the boundary condition but also because of the convex-down nature of the stress-strain relationship for $\varepsilon > \varepsilon_{el}$. Higher stress levels travel with higher velocity than lower stress levels which make the shock self sustained and independent of the exact form of the hysteresis prior the completion of phase transformation. From a physical point of view the phase transformation shock specifies the point of abrupt phase transition. For material points with $x \leq V_{ph}t$ the material is in the martensitic phase and the region $x \geq V_{ph}t$ is still in the austenitic phase.

The material properties used for the model problem are given in Table 1 and represent generic NiTi SMA properties. The length of the rod was taken to be 0.5m. The impact stress level used for the FEM runs was $\sigma_0 = 400MPa$ which corresponds to an impact strain of $\varepsilon_0 = -0.0635$ and is sufficient for the full completion of the phase transformation. The onset of phase transformation begins at $\sigma_{el} = -195MPa$ for a strain $\varepsilon_{el} = 2.78 \times 10^{-3}$. Given this, the speed of the transformation shock is $V_{ph} = 723m/s$ and the elastic shock travels with speed $V_{el} = 3294m/s$. All simulation were run for a total time of $100\mu s$ and at the completion of each run the numerical solution was compared with the analytical one.

Based on the first few numerical results (Figure 3) it can be observed that both the fixed and adaptive version of the FEM give numerical solutions with the expected two shocks - one elastic and another corresponding to the phase transformation. The smearing of the elastic shock is due to the numerical dissipation due to the time

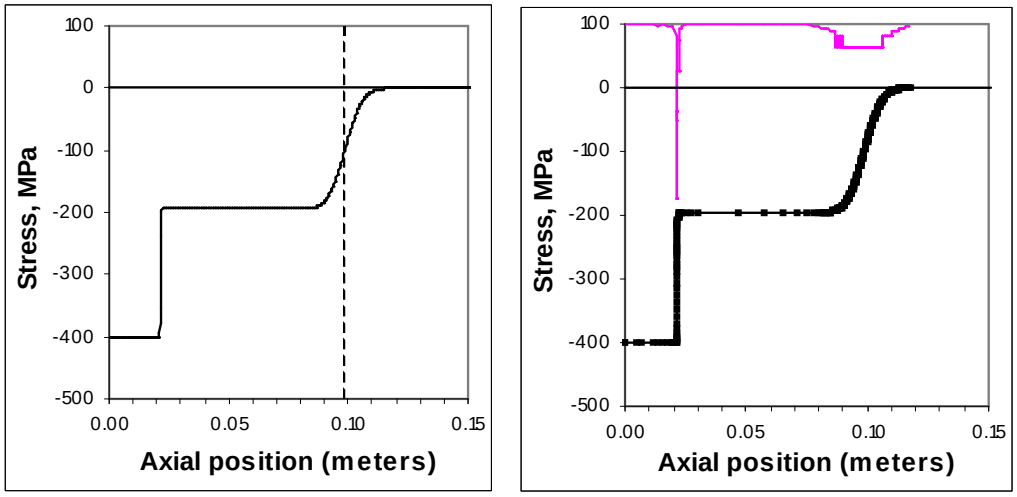

(a) (b)

Figure 3. Stress profile at $30\mu s$ for a fixed mesh with 2000 elements (a) and an adaptive mesh (b). Both are done for a time step $\tau = 0.1\mu s$. Mesh nodes in the adaptive mesh (b) are marked with black squares and the thin line at the top shows the density of elements.

Table 2. L^1 error in the displacement distribution at $T = 100\mu s$.

	N=2000	N=4000	N=8000	N=16000	N=32000
t=0.2 μs	$1.98 * 10^{-3}$	$1.99 * 10^{-3}$	$1.99 * 10^{-3}$		
t=0.1 μs	$1.31 * 10^{-2}$	$9.95 * 10^{-4}$	$9.97 * 10^{-4}$		
t=0.05 μs	$5.63 * 10^{-2}$	$1.26 * 10^{-2}$	$4.98 * 10^{-4}$	$4.99 * 10^{-4}$	
t=0.025 μs	$8.73 * 10^{-2}$	$8.74 * 10^{-3}$	$1.24 * 10^{-2}$	$2.49 * 10^{-4}$	$2.497 * 10^{-4}$

Table 3. L^1 error in the stress distribution along the rod at $T = 100\mu s$.

	N=2000	N=4000	N=8000	N=16000	N=32000
t=0.2 μs	$2.68 * 10^{-2}$	$2.75 * 10^{-2}$	$2.72 * 10^{-2}$		
t=0.1 μs	$3.42 * 10^{-2}$	$1.87 * 10^{-2}$	$1.91 * 10^{-2}$		
t=0.05 μs	$8.77 * 10^{-2}$	$2.95 * 10^{-2}$	$1.32 * 10^{-2}$	$1.34 * 10^{-2}$	
t=0.025 μs	$1.26 * 10^{-1}$	$5.61 * 10^{-2}$	$2.58 * 10^{-2}$	$9.41 * 10^{-1}$	$9.47 * 10^{-1}$

discretization scheme. The smearing effect can be eliminated by decreasing the time step for both the standard and the adaptive version of the FEM. The convergence of the standard FEM solver is shown on Tables 2 and 3. Due to the presence of discontinuities in the stress the relative error is measured in the L^1 norm. As seen from Table 2 the convergence rate for the displacements are of optimal order 1 for the linear elements used. A piecewise constant function on the other side has regularity $\frac{1}{2} - \delta$. That is, for every positive constant $\delta > 0$ the piecewise constant functions belong to the space $H_0^{\frac{1}{2}-\delta}(0,1)$. Therefore one cannot expect optimal convergence in the stresses and as seen from Table 3 the order of convergence is 0.5.

The adaptive FEM approach yields the same solutions as the standard FEM but at a much lower computational cost. For the same time steps for which the convergence of the fixed FEM was tested the adaptive meshing results in similar accuracy as seen from Table 4. A comparison in the computational performance of the fixed and adaptive FE methods is given in Table 5. The time step used is $\tau = 0.01\mu s$ and the number of elements for the fixed FEM is 16000. The adaptive solution is chosen so that it has comparable accuracy with the one for the fixed mesh solution. A comparison of the execution times for the fixed and adaptive methods shows that the adaptive procedure delivers an order of magnitude improvement in performance.

Table 4. L^1 error in the displacement distribution at $T = 100\mu s$.

τ	$0.2\ \mu s$	$0.1\ \mu s$	$0.05\ \mu s$	$0.025\ \mu s$
error, σ	$2.74 * 10^{-2}$	$1.93 * 10^{-2}$	$1.35 * 10^{-2}$	$9.54 * 10^{-3}$
error, u	$2.68 * 10^{-3}$	$1.64 * 10^{-3}$	$8.02 * 10^{-4}$	$4.34 * 10^{-4}$

Table 5. Execution times for fixed and adaptive meshes

Time	**Fixed Mesh**		**Adaptive Mesh**	
	Elements	Time (min)	Elements	Time (min)
$10\ \mu s$	16000	56	161	1:12
$20\ \mu s$	16000	113	199	2:37
$40\ \mu s$	16000	226	256	6:10
$80\ \mu s$	16000	451	301	15

3.3. Square pulse impact loading problem

A more realistic initial-boundary value problem is one for which, instead of step loading, the boundary condition is a square pulse, that is

$$\sigma_0(t) = \begin{cases} 0 & \text{for} \quad t \leq 0 \\ \sigma_0 & \text{for} \quad 0 < t < t_{pulse} \\ 0 & \text{for} \quad t \geq t_{pulse} \end{cases} \tag{10}$$

where t_{pulse} is the duration of the pulse. Due to the complicated constitutive response and boundary conditions there is no analytical solution to be compared with. Moreover, there are unresolved questions regarding the uniqueness of the weak solution for times $t > t_{pulse}$ when unloading takes place.

The stress level used for the numerical simulation is $\sigma_0 = 800MPa$ and the initial temperature is $T_R = 320\ ^\circ K > A^{of}$. The same material data as the one from the previous section is used with the exception that the value for the difference in the specific entropies is changed to $\rho\Delta s_0 = 3.5 \times 10^5$. The stress level is chosen so that the full adiabatic hysteresis loop can be realized. The pulse length is $t_{pulse} = 10\mu s$ and the time step is $t = 0.001\mu s$. The simulation time is $100\mu s$.

The evolution of the stress and temperature in the rod up to $90\mu s$ is shown in Figures 4 and 6. The two-shock solution for the stress is clearly visible at the end of the pulse load at $t = 10\mu s$ (Figure 4). The temperature profile (Figure 6) also has two shocks. The maximum temperature $T_0 = 378.8\ ^\circ K$ is achieved in the region of full phase transformation. The jump in the elastic shock is $T_{el} - T_R = 0.66\ ^\circ K$ and for this reason it is not clearly visible in the figure.

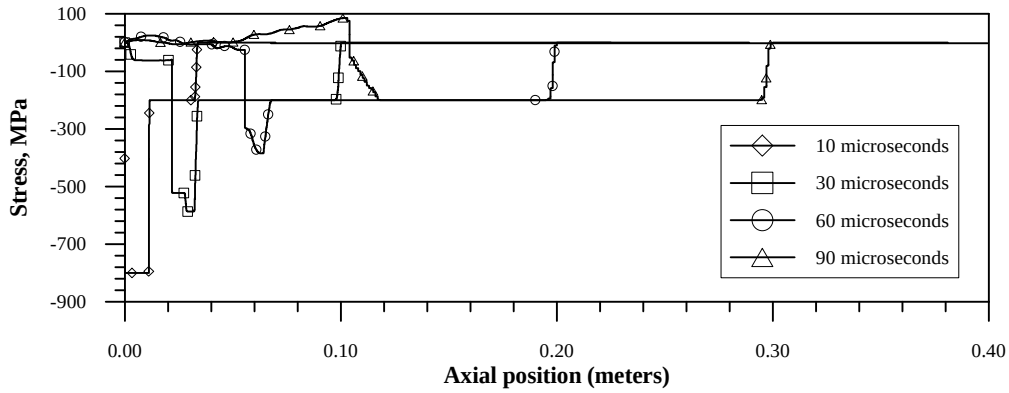

Figure 4. Stress profile at different instances of time for a square pulse in adiabatic loading

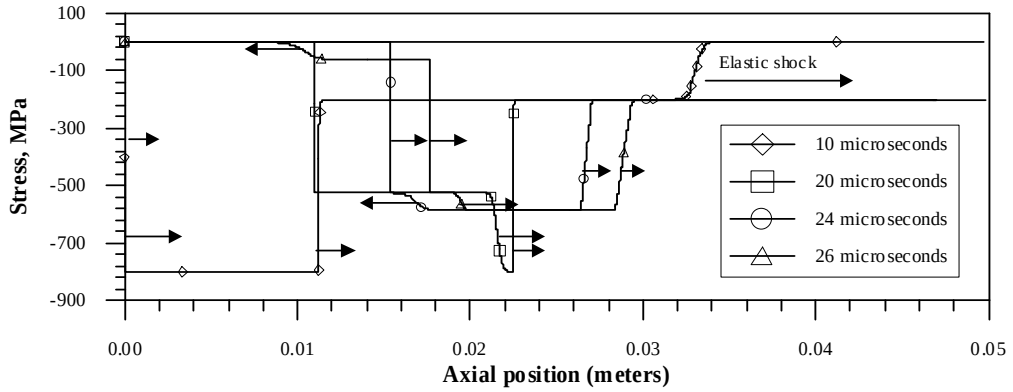

Figure 5. Magnified view near the left end. The unloading ($10\mu s$) produces two right-travelling shock waves ($20\mu s$). The faster unloading wave reflects off the transformation shock ($\approx 21\mu s$) and forms a left-travelling wave ($24\mu s$). What follows is a series of complicated reflections that gradually kill the initial non-linear shock.

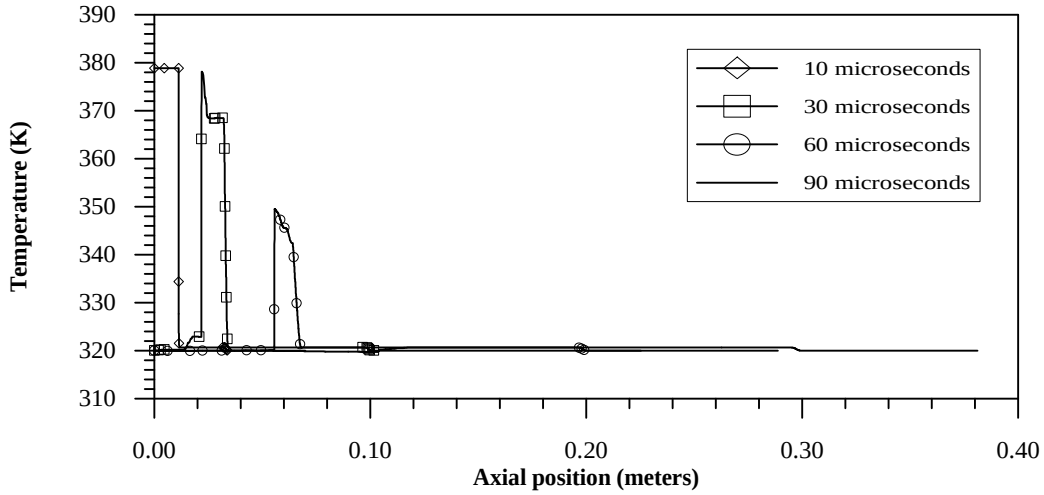

Figure 6. Temperature profile at various times. The jump at the forward transformation shock is $T_0 - T_{el} = 58.2\ ^\circ K$. The elastic shock is not visible clearly because of its small magnitude of $T_{el} - T_R = 0.66\ ^\circ K$.

The most noticeable feature observed in Figure 5 is the structure of the unloading pulse. Again a two wave shock structure is seen that corresponds to the initial elastic unloading and the following reverse transformation $M^t \rightarrow A$ as can be seen from the stress profile at 10 and $20\mu s$. Both unloading shocks travel faster than the forward phase transformation shock. When the faster unloading front catches up with the forward phase transformation shock ($t \approx 22\mu s$) a left-travelling reflection is generated. The left-travelling wave, as seen for $t = 24\mu s$, partially reflects from the slower unloading shock and partially continues ($t = 26\mu s$) until it reflects off the left end of the rod. A complicated series of reflection waves follows. The first reflection results in approximately 34% decrease of the peak stress level ($t = 24\mu s$). The picture becomes even more complicated when the slower unloading shock eventually catches up with the forward travelling phase transformation shock. Eventually the peak stress levels are reduced to values below σ_{el}, the critical stress corresponding to the onset of phase transformation. The temperature profile at $t = 90\mu s$ is hardly visible because the material is entirely in the elastic range and the temperature in the rod is very close to the reference temperature. The large amounts of latent heat generated during the initial loading phase are gradually consumed in the reverse transformation as the stress is reduced within the elastic limits.

For pulse loading it is physically meaningful to compute the energy dissipation due to the phase transformation. If $P(\tau)$ is the work done by the external forces at the left end of the rod from $t = 0$ up to $t = \tau$, $\mathcal{K}(\tau)$

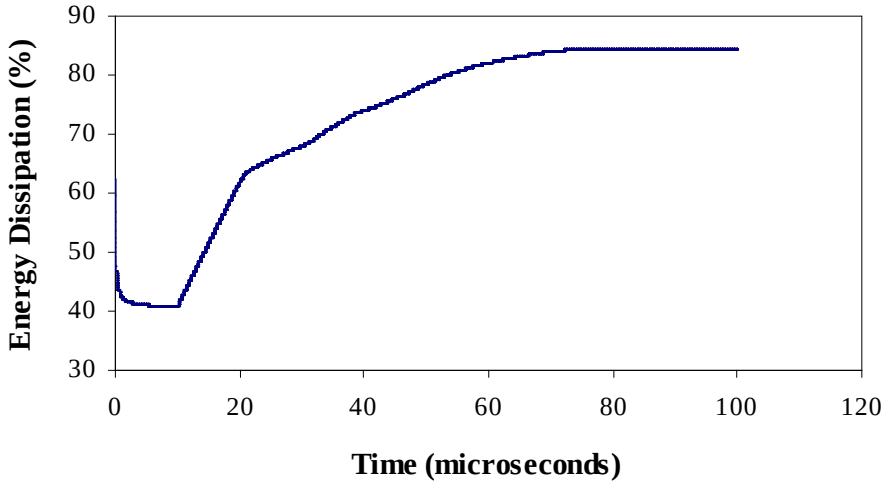

Figure 7. Energy dissipation for a 10 μs square pulse.

is the kinetic energy of the rod at time $t = \tau$ and $\mathcal{W}(\tau)$ is the stored elastic energy of the rod then the energy dissipation is defined by

$$D(\tau) = \frac{P(\tau) - (\mathcal{K}(\tau) + \mathcal{W}(\tau))}{P(\tau)} \tag{11}$$

The quantities P, $\mathcal{K}$ and $\mathcal{W}$ given can be easily computed numerically at each time step.

The calculations show (Figure 7) that the dissipation level goes from 40% at the end of the pulse ($t = 10\mu s$) to 64% at $t \approx 22\mu s$ when the faster unloading wave reflects off the forward travelling transformation wave. The high stress levels are then gradually reduced within the elastic limits. The energy dissipation reaches approximately 84% at 100 μs, shortly before the elastic front reaches the right end.

3.4. Dynamic Loading Experiment of an SMA rod

As a conclusion to the numerical study of wave propagation in NiTi SMA rods the adaptive FEM method is used to analyze actual experimental data from an impact test. The test setup and the experiment are presented in [6]. The test have been performed on a long NiTi SMA spceimen using a split-Hopkinson bar device under conditions of detwinning of martensite. Recordings of the strains from 5 strain gauges mounted on the SMA specimen have been obtained.

Based on the experimental results it has been determined that the most adequate model of the stress-strain behavior in detwinning conditions is a phenomenological model. The model utilizes a polynomial curve fit for the loading part of the hysteresis. The unloading is assumed linear elastic. This approach allows for correct modelling of the inelastic detwinning deformation which does not exhibit an initial elastic response but exhibits a gradually changing stiffness. The precise modelling of the stiffness is important as it directly influences the propagation speed of the nonlinear waves in the SMA rod.

The results of the test along with the adaptive FE simulation are shown on Figure 8. The simulation covered $200\mu s$ which was the time needed by the wave generated in the SMA bar to traverse its length. It can be observed that the timing of the waves as well as the peak strain levels of the numerical simulation are in good agreement with the experimental results.

4. CONCLUSIONS

The problem of dynamic loading of one-dimensional polycrystalline SMA rods has been explored using fixed and adaptive Finite Element techniques. FEM simulations were performed for SMAs experiencing both pseudoelastic phase transformation as well as detwinning deformations. Computational solutions were shown to coincide with

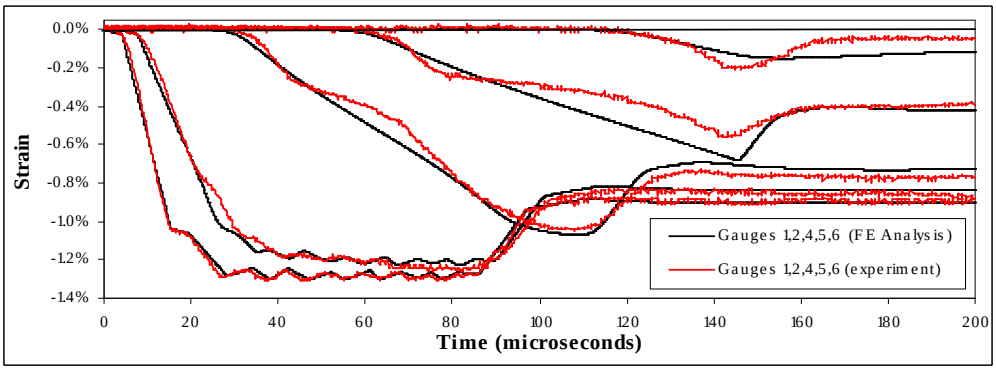

Figure 8. An adaptive FE analysis of experimental data under isothermal conditions and a curvefit of the hysteresis.

known analytical results. Nonlinear shock formation and velocities were captured correctly by the simulations. The displacements and stresses obtained by the standard semi-discrete FEM approach were shown to converge to the analytical values. The convergence in the the stresses was of the the best possible order given the regularity of the piecewise constant solution.

The standard FEM approach for hyperbolic problems was complemented by an adaptive mesh refinement technique. The utilization of the Zienkiewicz-Zhu error indicator lead to an order of magnitude decrease of the computational time without compromising the accuracy of the numerical solution. Energy dissipation calculations for stress-induced phase transformation showed that the strain energy can be reduced by 80-90% which suggests that SMAs can be used effectively as shock-absorption devices. Accurate predictions of actual experimental data were also obtained. Both the wave timings, shape and peaks were modelled within experimental error.

The material and environmental conditions used in the Hopkinson bar experiment used to correlate with the numerical simulations correspond to a detwinning deformation of the martensitic phase, but the methods can be easily adapted to stress induced martensitic transformation in tests at higher temperatures. Such experiments can be used to validate the numerical approach over a much broader range of thermomechanical paths. Theoretical work can also be extended to more realistic 2-D and 3-D geometries. Complicated SMA components and structures can be simulated to better understand the nonlinear wave propagation phenomena as well as the practical aspects of their energy dissipation capabilities. More refined models which incorporate both detwinning and pseudoelastic deformations simultaneously and also predict accurately the smooth hysteresis of the detwinning deformation will be extremely helpful in further studies of wave propagations in polycrystalline SMAs and are currently under consideration.

Acknowledgements

The authors would like to acknowledge the financial support of the Air Force Office of Scientific Research, Grant No. F49620-01-1-0196.

References

[1] H. Funakubo, *Shape Memory Alloys*, Gordon and Bleach, New York, 1987.

[2] Y.-C. Chen and D. C. Lagoudas, "Impact induced phase transformation in shape memory alloys," *J. Mech. Phys. Solids* **48**(2), pp. 275–300, 2000.

[3] D. Lagoudas, Z. Bo, and M. Qidwai, "A unified thermodynamic constitutive model for sma and finite element analysis of active metal matrix composites," *Mechanics of Composite Structures* **3**, pp. 153–179, 1996.

[4] A. Bekker, J. Victory, P. Popov, and D. Lagoudas, "Impact induced propagation of phase transformation in a shape memory alloy rod," *International Journal of Plasticity* **18**(11), pp. 1425–1647, 2002.

[5] J. C. Jimenez-Vicktory, "Dynamic analysis of impact induced phase transformation in shape memory alloys using numerical techniques," aerospace engineering, Texas A&M University, December 1999.

[6] D. Lagoudas, K. RaviChandar, K. Sarh, and P. Popov, "Dynamic loading of polycrystalline shape memory alloy rods," *Mechanics of Materials* , 2003, in press.

[7] E. Oberaigner, K. Tanaka, and F. Fischer, "Investigation of the damping behavior of a vibrating shape memory alloy rod using a micromechanical model," *Smart Materials and Structures* (3), pp. 456–463, 1996.

[8] Z. Bo and D. C. Lagoudas, "Thermomechanical modeling of polycrystalline SMAs under cyclic loading, part I: theoretical derivations," *International Journal of Engineering Science* **37**, pp. 1089–1140, 1999.

[9] L. C. Brinson, "One-dimensional constitutive behavior of shape memory alloys: Thermomechanical derivation with non-constant material functions and redefined martensite internal variable," *J. of Intell. Mater. Syst. and Struct.* **4**, pp. 229–242, 1993.

[10] D. Lagoudas and S. Shu, "Residual deformations of active structures with sma actuators," *International Journal of Mechanical Sciences* **41**, pp. 595–619, 1999.

[11] R. Abeyaratne and J. K. Knowles, "Continuum model of a thermoelastic solid capable of undergoing phase transformation," *J. Mech. Phys. Solids* **41**, pp. 541–571, 1993.

[12] N. Siderey, E. Patoor, M. Berveiller, and A. Eberhardt, "Constitutive equations for polycrystalline thermoelastic shape memory alloys. part i. intragranular interactions and behavior of the grain," *International Journal of Solids and Structures.* **36**, pp. 4289–4315, 1999.

[13] Q. P. Sun and K. C. Hwang, "Micromechanics modeling for the constitutive behavior of polycrystalline shape memory alloys — I. Derivation of general relations," *J. Mech. Phys. Solids* **41**(1), pp. 1–17, 1993.

[14] M. A. Qidwai and D. C. Lagoudas, "On thermomechanics and transformation surfaces of polycrystalline shape memory alloy materials," *International Journal of Plasticity* **16**(10-11), pp. 1309–1343, 2000.

[15] O. Zienkiewicz and J. Zhu, "A simple error estimator and an adaptive procedure for practical engineering analysis," *International Journal for Numerical Methods in Engineering* **24**, pp. 337–357, 1987.

[16] K. Graff, *Wave Motion in Elastic Solids*, Oxford University Press, London, 1975.

[17] L. Malvern, *Introduction to the Mechanics of a Continuous Medium*, Prentice-Hall Inc., Englewood Cliffs, N.J., 1977.

[18] J. N. Reddy, *An Introduction to the Finite Element Method*, McGraw-Hill, 1993.

[19] M. A. Qidwai and D. C. Lagoudas, "Numerical implementation of a shape memory alloy thermomechanical constitutive model using return mapping algorithms," *International Journal for Numerical Methods in Engineering* **47**, pp. 1123–1168, 2000.